

Precise Measurements of CH Maser Emission and Its Abundance in Translucent Clouds

NINGYU TANG,^{1,2} DI LI,^{2,3} GAN LUO,⁴ CARL HEILES,⁵ SHENG-LI QIN,⁶ JUNZHI WANG,⁷ JIFENG XIA,² AND LONGFEI CHEN²

¹*Department of Physics, Anhui Normal University, Wuhu, Anhui 241002, China*

²*National Astronomical Observatories, CAS, Beijing 100012, China*

³*NAOC-UKZN Computational Astrophysics Centre, University of KwaZulu-Natal, Durban 4000, South Africa*

⁴*School of Astronomy and Space Science, Nanjing University, 163 Xianlin Road, Nanjing 210023, China*

⁵*Department of Astronomy, University of California, Berkeley, 601 Campbell Hall 3411, Berkeley, CA 94720-3411, USA*

⁶*Department of Astronomy, Yunnan University, Kunming 650091, China*

⁷*Shanghai Astronomical Observatories, CAS*

ABSTRACT

We present high-sensitivity CH 9 cm ON/OFF observations toward 18 extra-galactic continuum sources that have been detected with OH 18 cm absorption in the Millennium survey with the Arecibo telescope. CH emission was detected toward six of eighteen sources. The excitation temperature of CH has been derived directly through analyzing all detected ON and OFF velocity components. The excitation temperature of CH 3335 MHz transition ranges from -54.5 to -0.4 K and roughly follows a log-normal distribution peaking within $[-5, 0]$ K, which implies overestimation by 20% to more than ten times during calculating CH column density by assuming the conventional value of -60 or -10 K. Furthermore, the column density of CH would be underestimated by a factor of 1.32 ± 0.03 when adopting local thermal equilibrium (LTE) assumption instead of using the CH three hyperfine transitions. We found a correlation between the column density of CH and OH following $\log N(\text{CH}) = (1.80 \pm 0.49) \log N(\text{OH}) - 11.59 \pm 6.87$. The linear correlation between the column density of CH and H₂ is consistent with that derived from visible wavelengths studies, confirming that CH is one of the best tracers of H₂ component in diffuse molecular gas.

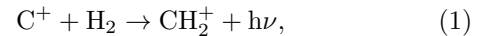
Keywords: ISM: clouds — ISM: evolution — ISM: molecules.

1. INTRODUCTION

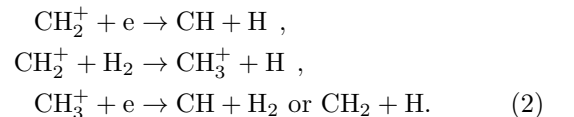
The CH radical, a simple hydride, is the first molecule detected in the interstellar medium (ISM) through the visible $A^2\Delta-X^2\Pi$ 4300-Å absorption (Dunham 1937; Swings & Rosenfeld 1937; McKellar 1940). Absorption observations toward early-type stars in the visible wavelength (4300-Å) show the ubiquitous existence of CH in the ISM (e.g., Federman 1982; Danks et al. 1984; Sheffer et al. 2008), and the visible 4300-Å line has been used extensively to identify the foreground cold gas components at a spectral resolution of 0.3 to 0.6 km s⁻¹ (e.g., Crawford 1995; Crane et al. 1995). The lack of bright, early-type background star is a major limitation on the usage of the 4300-Å line (Liszt & Lucas 2002).

The $^2\Pi_{1/2}$, J=1/2 Λ -doubling radio lines of CH (3264, 3335 and 3349 MHz; see Figure 1 for details) have been widely used in studying CH abundance and ISM evolution. In the past decades, radio studies reveal that the 3.3 GHz (9 cm) emissions exist in various star-forming environments such as diffuse and translucent cloud (e.g., Lang & Wilson 1978; Sandell et al. 1980, 1981; Mattila 1986; Magnani & Onello 1993; Sakai et al. 2012), dark cloud (e.g., Jacq et al. 1987), and molecular outflows (e.g., Sandell et al. 1988; Magnani et al. 1992).

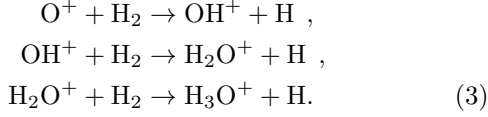
Chemically, CH is the first generation molecule in the carbon chemical network. Starting from C⁺ (e.g., Federman et al. 1984),



CH is then synthesized by the following reactions



Similar to CH, hydroxyl (OH) is the first generation molecule in the oxygen chemical network which initiates from O^+ . The reactions could happen as follows



H_2O^+ and H_3O^+ then recombine with ambient electrons to form OH.

Based on the above facts, both CH and OH could be adequate for tracing H_2 , particularly in the HI- H_2 transition zone (Li et al. 2015, Xu & Li 2016). Noted that C^+ is produced by the photoionization of atomic carbon, while the O^+ is produced through charge exchange between O and H^+ , in which H^+ originates from cosmic ray ionization of H.

The emission of CH and OH are generally weak (usually tens of mK in diffuse and translucent cloud), which requires a long integration time. Furthermore, the derivation of column density (therefore abundance) requires an exact value of excitation temperature and optical depth. The combination of ON (absorption) and OFF (emission) observations toward continuum source provides direct measurements of these two parameters. This method has been widely applied for quantifying physical properties of HI (e.g., Dickey et al. 1983), OH (e.g., Dickey et al. 1981), and HCO^+ (e.g., Lucas & Liszt 1996; Luo et al. 2020).

Efforts have been taken to directly quantify the excitation of CH through ON/OFF observations toward continuum sources since the 1970s. A series of Galactic continuum sources (e.g., Cas A*) and extra Galactic sources (e.g., 3C123) were surveyed with the Onsala Space Observatory 25.6 m telescope (Rydbeck et al. 1976; Hjalmarsen et al. 1977) and Effelsberg 100-m telescope (Genzel et al. 1979). Results based on these observations reveal that the T_{ex} of CH is inverted and ranges from -60 to -9 K but with relatively large uncertainty. The T_{ex} value of -10 K or -60 K derived from these observations is usually adopted to calculate the CH column density from 3335 MHz emission. This assumption may cause large deviation of calculating CH column density if $|T_{ex}| < 3$ K (Dailey et al. 2020). Recent modeling of CH 9 cm and 149 μ m data toward four high-mass star-forming regions imply an extreme value, $T_{ex} \sim -0.3$ K (Jacob et al. 2021), which would lead to deviation of CH column density by a factor of 8.

To further investigate T_{ex} of CH in high sensitivity and to investigate the relationship between CH and OH in tracing H_2 , sensitive CH and OH ON/OFF spectra toward continuum sources are necessary. The Millennium survey took a high sensitive HI absorption sur-

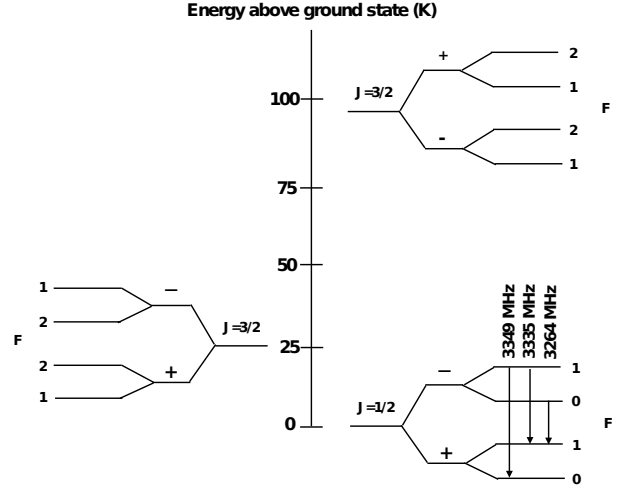


Figure 1. Energy-level diagram of 3 lowest CH $^2\Pi$ rotational transitions. The 3335, 3264, and 3349 MHz transitions happen between different hyperfine F levels of the state $^2\Pi_{1/2}, J = 1/2$. LTE intensity ratios between these transitions are $I(3335):I(3264):I(3349)=2:1:1$. The spacing of the Λ -doubled and hyperfine levels are not to scale.

vey toward 79 continuum sources with Arecibo telescope (Heiles & Troland 2003a,b). Analysis results of corresponding OH data of this survey are present in Li et al. (2018a) and Nguyen et al. (2018). In this paper, we describe our results of a follow-up CH survey toward 18 sightlines with detected OH absorption using the Arecibo telescope.

The paper is organized as follows. The observations and analysis are described in section 2 and 3, respectively. The derived CH properties are shown in section 4. We described the relationship between CH and OH in section 5 and the relationship between CH and H_2 in section 6. Summary is presented in section 7.

2. OBSERVATIONS

We have chosen 18 sources in the Millennium survey that have both HI and OH absorption detections (Li et al. 2018a). Figure 2 shows the spatial distribution of the observed sources overlaid on Planck extinction map.

Three Λ -doubling lines of CH in the $^2\Pi_{1/2}, J=1/2$ ground state were obtained with the Arecibo S-band receiver using the Wideband Arecibo Pulsar Processor (WAPP) backend in 2016 and 2019. The beam size (full width at half maximum, FWHM) is ~ 1.5 arcmin at 3.3 GHz. The rest frequencies are 3335.481 MHz ($F=1-1$) for the main line, 3263.794 MHz ($F=0-1$) and 3349.193 MHz ($F=1-0$) for the two satellite lines. Each spectrum

has a bandwidth of 3.125 MHz in 8192 channels, resulting in a velocity resolution of 0.034 km s^{-1} . The data were then smoothed into 0.068 km s^{-1} to be comparable with OH data in Li et al. (2018a).

During April and May 2016, observations were taken toward 18 sources and one OFF position (2 arcmin offset from the source in the north). The integration time is 10 minutes toward both ON and OFF positions. The system temperature is $\sim 28 \text{ K}$, resulting in a reduced root-mean-square (rms) of $\sim 28 \text{ mK}$ (antenna temperature) in the OFF spectrum. CH lines were detected toward six sources, namely 3C123, 3C131, 3C133, 3C154, T0526+24, and T0629+10. During February and June 2019, we were able to observe 5 (3C123, 3C131, 3C133, 3C154, and T0629+10) of the above 6 sources with an ON position and 4 OFF positions (2 arcmin offset in the East, North, West, and South from the sources) in higher sensitivity. Twelve and three cycles of five-minute scans were taken for ON and each OFF position, respectively. This leads to a final rms of $\sim 9 \text{ mK}$ in the OFF spectrum.

3. ANALYSIS

3.1. Radiation Transfer

With the assumption of invariant CH distribution toward ON and OFF positions, the obtained antenna temperature $T_A(\nu)$ after removing continuum baseline for ON/OFF observations are described by

$$T_A^{\text{ON}}(\nu) = \eta_b \eta_f (T_{\text{ex}} - T_{\text{bg}} - \eta_{\text{cf}} T_C^{\text{b}}) (1 - e^{-\tau_\nu}) \quad (4)$$

$$T_A^{\text{OFF}}(\nu) = \eta_b \eta_f (T_{\text{ex}} - T_{\text{bg}}) (1 - e^{-\tau_\nu}) \quad (5)$$

in which T_{ex} and τ_ν are the excitation temperature and optical depth of the foreground molecular cloud, respectively. The brightness continuum temperature T_{bg} includes the contribution of both CMB (2.73 K) and Galactic synchrotron background, which is estimated as $\sim 0.07 \text{ K}$ at 3.3 GHz by applying spectral index of -2.8 from the 408 MHz survey (Haslam et al. 1982). η_b is the main beam efficiency. It is 0.57 ± 0.02 and 0.40 ± 0.04 before and after 2017 September 20, when the Arecibo telescope was hit by a hurricane. η_f is the beam filling factor of the cloud and is assumed as 1.

η_{cf} and T_C^{b} are the continuum source filling factor of the beam and brightness temperature of the background continuum sources, respectively. For point sources, $\eta_b \eta_{\text{cf}} T_C^{\text{b}}$ equals T_C^{A} , which is the antenna temperature of the point continuum source.

For the sources with 4 OFF positions, their OFF spectra were obtained by averaging the spectra of 4 OFF

positions. By combining the equation 4 and 5, the excitation temperature T_{ex} and optical depth profile $e^{-\tau_\nu}$ can be determined.

3.2. Spectral Line Fitting

Following the method in Heiles & Troland (2003a), each profile was fitted with multiple Gaussian components to reach minimum variance. Firstly, we estimate the rms of each spectrum in the emission free velocity range (e.g., -10 to -5 km s^{-1} along 3C123). An effective decomposed component was generally certificated by the 3σ criteria except for the -2.2 km s^{-1} velocity component of the 3335 OFF spectrum toward 3C154. There are 3 cases according to the strength of CH intensity.

1. CH emission is detected in both the ON and OFF spectrum and has a significant S/N ratio in the ON-OFF spectrum. This is the case for the 3335 MHz spectra of 3C123, 3C133, and T0629+10. For these sources, we first applied Gaussian decomposition to the optical depth profile, then the fitted central velocities of all components were fixed as initial values of the ON and OFF spectral fitting.
2. CH emission is detected in both the ON and OFF spectrum but without significant detection (3σ level) in the ON-OFF spectrum. This is the case for the 3335 MHz spectra of 3C131 and T0526+24. For these sources, we applied Gaussian decomposition to the ON profile, then the fitted central velocities were fixed as initial values of the OFF spectral fitting.
3. CH emission is detected in the ON spectrum and is absent in the OFF spectrum. This is the case for the 3335 MHz spectra of the 3C154 component with a center velocity of -1.3 km s^{-1} . Gaussian decomposition was adopted to the ON spectrum only.

The Gaussian fitting results of three CH transitions toward 3C123 are shown in Figure 3 as an example. The fitting results of the rest sources can be found in Figure 9. The derived physical parameters (line central velocity, line width, optical depth, excitation temperature, and column density) are presented in Table 1 and Table 2. A total of 12, 13, and 15 Gaussian components of 3264, 3335, and 3349 MHz lines are identified, respectively.

4. PHYSICAL PROPERTIES OF CH

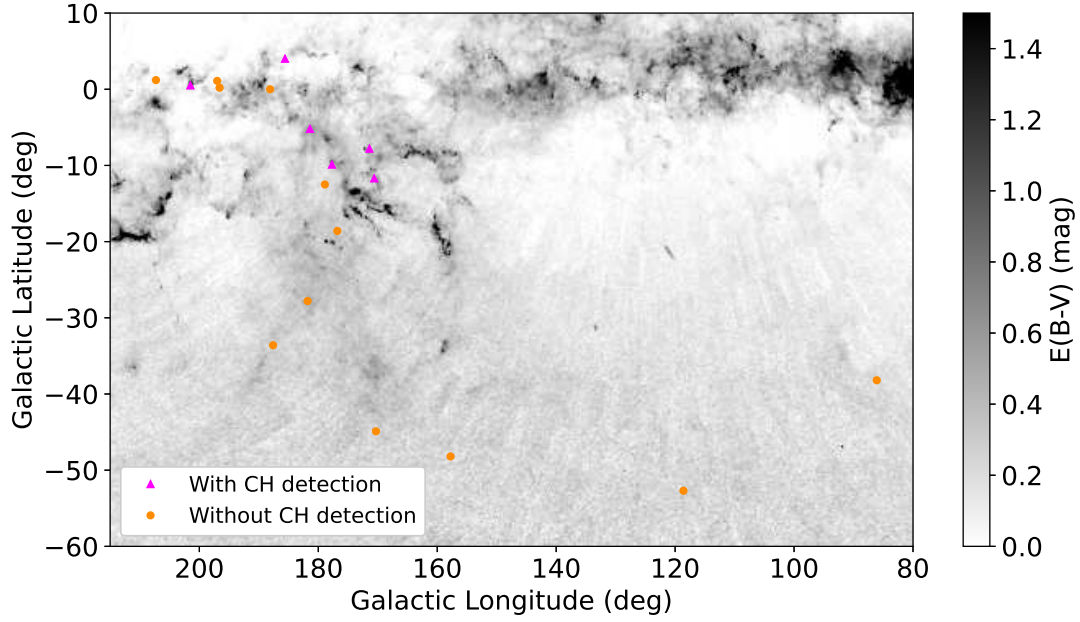


Figure 2. Spatial distribution of observed 18 sources overlaid on the Planck extinction map. The value of color excess $E(B-V)$ ranges from 0 (white) to 1.5 (black) mag.

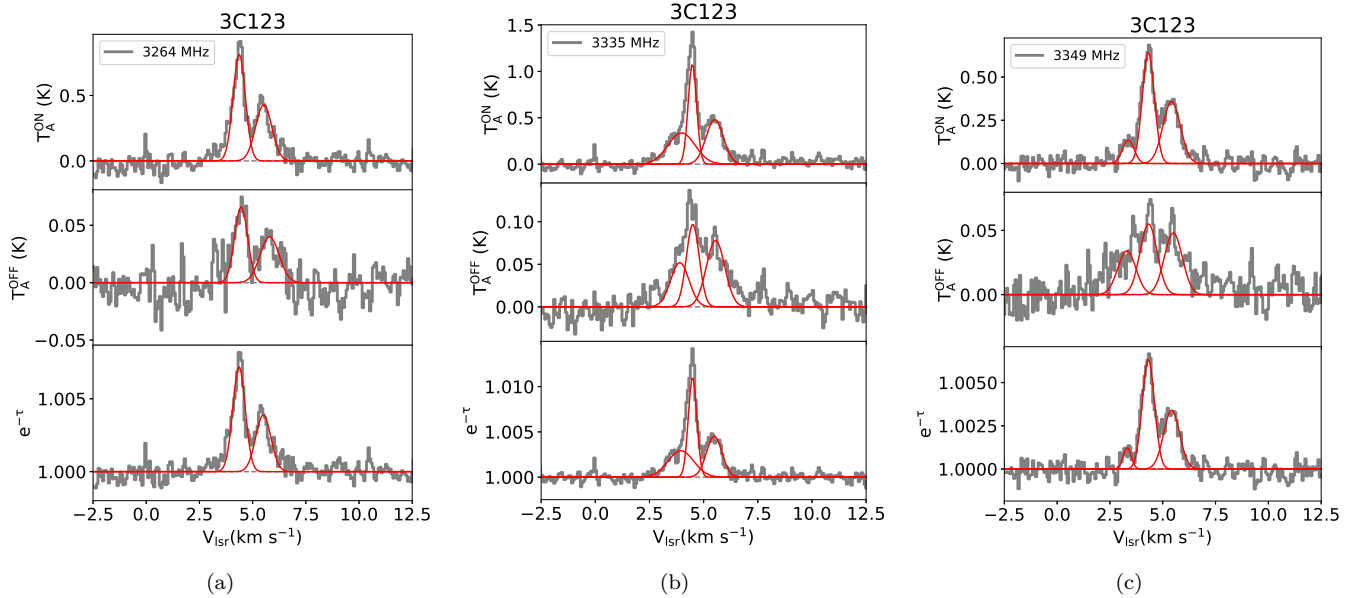


Figure 3. Spectra and Gaussian decomposition results of 3C123 for 3264 (a), 3335 (b) and 3349 MHz (c) line. The top and middle panel represents the ON and OFF profile (antenna temperature) after removing the continuum level. The bottom panel represents the profile of optical depth, $e^{-\tau}$.

The physical parameters were calculated based on the fitting results of Gaussian components. They are described as follows.

4.1. Excitation Temperature and Optical Depth

The ON/OFF observations provide a direct measurement of excitation temperature T_{ex} and optical depth τ in the case of 1 and 2. For case 3, lower limits are derived due to the absence of CH detection in the OFF position.

Due to the limitation of a small sample number, the Monte Carlo method is introduced to estimate the probability distribution of physical parameters. As shown in the histogram in Figure 4(a), the excitation temperature peaks of CH 3335 MHz and 3264 MHz lines are in the range of $[-5, 0]$ K, which is consistent with that found by combining the optical and radio CH observations (Dailey et al. 2020). For CH 3349 MHz line, the excitation temperature peak is in more negative values with range of $[-10, -5]$ K. Our results confirm that the excitation of CH 9 cm transition is always strongly inverted (negative T_{ex} value). The distributions of excitation temperature T_{ex} with range of $(-62, 15)$ K are fitted with a log-normal function, which follows

$$f(x) = \frac{a}{(15 - T_{\text{ex}})\sigma} e^{-\frac{(\ln(15 - T_{\text{ex}}) - \mu)^2}{2\sigma^2}}, \quad (6)$$

where a , μ and σ are three free parameters. The fitting results of a , μ and σ for 3335, 3264 and 3349 MHz lines are (1.7, 3.2, 0.4), (1.2, 3.0, 0.3) and (1.2, 3.1, 0.3) respectively.

As shown in Figure 4(b), the CH lines are optically thin in our sample (with maximum $|\tau|$ value of 0.034). The optical depth of 3264 MHz, 3335 MHz, and 3349 MHz are in the range of $(-36.7 \sim -2.3) \times 10^{-3}$, $(-33.5 \sim -2.9) \times 10^{-3}$, and $(-25 \sim 0.2) \times 10^{-3}$, respectively.

The comparison with previous CH 3335 MHz observations of 3C123 and 3C133 is shown as follows.

3C123: As a bright calibrator, 3C123 has been observed under ON/OFF mode for many times in the last 45 years. With the Onsala Space Observatory 25.6m telescope, T_{ex} was estimated as -10 K in Rydbeck et al. (1976) and -9 K in Hjalmarsen et al. (1977). Liszt & Lucas (2002) determined a consistent T_{ex} value of -10.7 ± 3.2 K with the NRAO 43m telescope. Due to sensitivity limitation of these observations, only one component centering at ~ 4 km s $^{-1}$ was detected. Genzel et al. (1979) identified two velocity components (centering at 4.5 and 5.5 km s $^{-1}$) with the Effelsberg 100 m telescope, resulting in a T_{ex} of -60 ± 30 K of the 3335 MHz main line.

With improved sensitivity and spectral resolution of the Arecibo telescope, we have identified 3 velocity com-

ponents (centering at 4.0, 4.5 and 5.5 km s $^{-1}$). The corresponding T_{ex} values are -54.5 ± 12.1 , -10.5 ± 2.9 and -33.2 ± 6.8 K, respectively. The first two values are consistent with previous studies. These results suggest that the beam size and sensitivity are critical for determining the CH excitation temperature.

3C133: It was observed by Liszt & Lucas (2002) but there is no clear implication of T_{ex} value toward this source. In this work, we derived T_{ex} value of -13.3 ± 2.4 K toward the 7.7 ± 0.0 km s $^{-1}$ component. Compared to the 3335 MHz main line, the OFF spectrum of 3349 MHz line shows an extra component with central velocity of 8.5 ± 0.1 km s $^{-1}$. The origin of this extra velocity component is difficult to understand now. Further interferometric observations with high spatial resolution, e.g., VLA are needed.

4.2. CH Column Density

The transition energy between the lowest two excitation states ($J=3/2$ and $J=1/2$) is 25.5 K. While the critical density is 10^6 cm $^{-3}$ (Sakai et al. 2012), meaning that almost all CH molecules are located in the $J=1/2$ Λ -type doubling levels in our sightlines. With the assumption of local thermal equilibrium (LTE), the CH populations at different F levels follow the statistical population distribution since the excitation temperatures of 3264, 3335, and 3349 MHz lines are same. The total CH column density under LTE condition can be derived by (Genzel et al. 1979)

$$N(\text{CH})^{\text{LTE}} = 2.82 \times 10^{14} \text{ cm}^{-2} \delta T_{\text{ex}} \Delta V \tau, \quad (7)$$

where ΔV is the FWHM of CH line respectively. The statistical ratio δ is 1 for the 3335 MHz line and 2 for the 3264 and 3349 MHz line (Rydbeck et al. 1976).

As presented in section 4.1, excitation temperatures of 3 transitions are totally different even when uncertainties are considered, indicating the invalidity of LTE assumption. In this case, the total column density should be calculated through (Suutarinen et al. 2011)

$$N(\text{CH}) = N_{u,1} \left(1 + e^{\frac{T_{11}}{T_{\text{ex},11}}} + \frac{1}{3} e^{\frac{T_{10}}{T_{\text{ex},10}}} + \frac{1}{3} e^{\frac{T_{11}}{T_{\text{ex},11}}} - \frac{T_{01}}{T_{\text{ex},01}} \right), \quad (8)$$

where $N_{u,1}$ is the upper $F=1$ column density of the $J=1/2$ ground state and is calculated from the 3335 MHz data, $N_{u,1} = N(\text{CH})^{\text{LTE}}/2$. $T_{\text{ex},11}$, $T_{\text{ex},10}$ and $T_{\text{ex},01}$ are the excitation temperature of 3335, 3349 and 3264 MHz line respectively.

With the direct measurement of both main line and satellite lines of CH, we are able to compare the estimating results from both Equation 7 and 8. Only 10 velocity components have optical depth and excitation

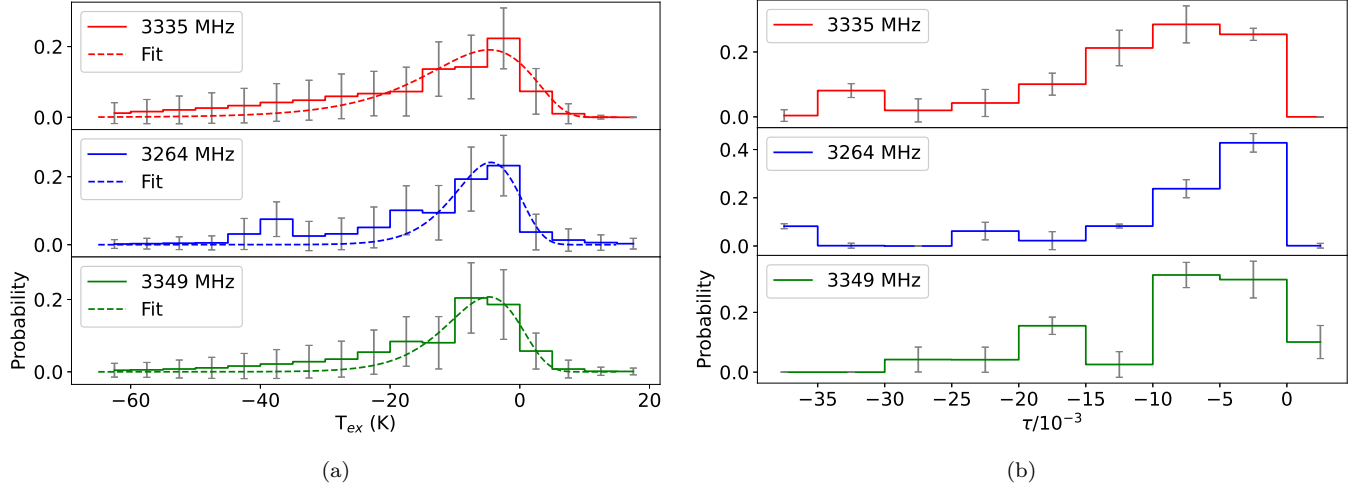


Figure 4. Histogram of excitation temperature (a) and optical depth (b) of CH transitions. The dashed lines in figure (a) represent fitting results of excitation temperature distribution. The two large T_{ex} values (300 and -754 K) of 3349 line are not included in the figure (a).

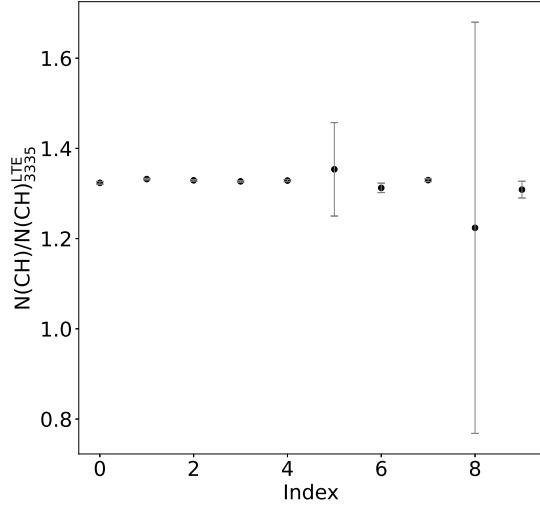


Figure 5. Ratio between $N(\text{CH})$ and $N(\text{CH})_{3335}^{\text{LTE}}$ for 10 CH components. The ninth point with large error corresponds to the T0629+10 component centering at 6.1 km s^{-1} , which has $T_{\text{ex}}^{3335} = -0.9 \pm 4.1 \text{ K}$.

temperature measurements of three CH lines. As shown in Fig. 5, the ratios between $N(\text{CH})$ from Equation 8 and $N(\text{CH})_{3335}^{\text{LTE}}$ based on 3335 MHz data and Equation 7 are almost constant, with a value of 1.32 ± 0.03 . This implies that the previous studies of calculating $N(\text{CH})$ based on 3335 MHz data alone by adopting LTE assumption would underestimate $N(\text{CH})$ by 32%.

The column density of all the 12 CH 3335 MHz components are shown in Table 1. The $N(\text{CH})$ for the two velocity components 3C123 (4.0 km s^{-1}) and 3C154 (-2.2 km s^{-1}) are estimated from $N(\text{CH})_{3335}^{\text{LTE}}$ by multiplying a factor of 1.32 ± 0.03 . $N(\text{CH})$ ranges over two orders of

magnitude in our sample, from 1.3×10^{12} to $1.4 \times 10^{14} \text{ cm}^{-2}$.

4.3. Implication for $N(\text{CH})$ from CH 3335 MHz Emission

Previous CH 3335 MHz observations (see section 6 for details) always adopted a fixed temperature $T_{\text{ex}} = -10$ or -60 K for the calculation of $N(\text{CH})$ through $N(\text{CH}) \propto (T_{\text{ex}}/(T_{\text{ex}} - T_{\text{bg}}))W(\text{CH})$, in which $W(\text{CH})$ is the integrated intensity of CH 3335 MHz emission.

We define R as the ratio between $N(\text{CH})$ and $N(\text{CH}; T_{\text{ex}} = -60 \text{ K})$ calculated by adopting $T_{\text{ex}} = -60 \text{ K}$, namely, $R = N(\text{CH})/N(\text{CH}; T_{\text{ex}} = -60 \text{ K})$. As shown in Figure 6, the value of R decrease monotonously as a function of T_{ex} . The adoption of $T_{\text{ex}} = -60 \text{ K}$ and $T_{\text{ex}} = -10 \text{ K}$ would overestimate $N(\text{CH})$ by a factor of 2 and 1.6 respectively compared to that of $T_{\text{ex}} = -2.8 \text{ K}$. A larger negative T_{ex} value ($-2.8 \text{ K} < T_{\text{ex}} < 0 \text{ K}$) leads larger deviation. The overestimation factor is 9.9 and 8.2 for $T_{\text{ex}} = -0.3 \text{ K}$, which is found in Jacob et al. (2021).

5. RELATIONSHIP BETWEEN CH AND OH

The two simple hydrides, CH and OH are two of the most popular molecular tracers in diffuse and translucent clouds. The abundance and relationship between the two species have been investigated by a lot of studies in both radio and visible wavelengths.

Rydbeck et al. (1976) obtained CH 9 cm and OH 18 cm absorption and emission spectra toward strong continuum sources and derived $N(\text{CH})/N(\text{OH}) = 0.06$ for compact molecular clouds and $N(\text{CH})/N(\text{OH}) = 0.4$ for the dilute HI clouds. Liszt & Lucas (2002)

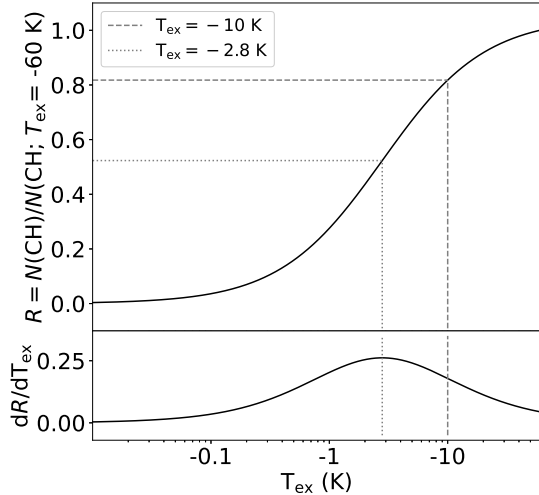


Figure 6. The value of $R = N(\text{CH})/N(\text{CH}; T_{\text{ex}} = -60 \text{ K})$ (upper panel) and its first-order derivative (lower panel) as a function of excitation temperature. The background temperature is adopted as $T_{\text{bg}} = 2.8 \text{ K}$ in our calculation. When $T_{\text{ex}} = -2.8 \text{ K}$ (grey dotted line), the R value is 0.52 and the dR/dT_{ex} value reaches its maximum. The corresponding R value is 0.82 when $T_{\text{ex}} = -10.0 \text{ K}$ (grey dashed line).

summarized the CH observations of CH B-X 3890 Å and C-X 3150 Å (Federman et al. 1994; Crane et al. 1995) and the corresponding electronic OH A-X and D-X observations (Roueff 1996; Felenbok & Roueff 1996) along 4 sightlines (Table 1 of Liszt & Lucas (2002)), in which they found the $N(\text{CH})/N(\text{OH})$ ratio is 0.33 ± 0.10 . Weselak et al. (2009) and Weselak et al. (2010) obtained CH and OH column densities through CH B-X data at 3886 and 3890 Å and OH A-X data at 3078 Å and 3083 Å toward a total of 20 translucent sightlines (Liszt & Lucas (2002) adopted some of their data), in which the OH data toward 4 sightlines were obtained from Roueff (1996), Felenbok & Roueff (1996) and Boissé et al. (2005). They found the column density of CH and OH have positive correlation, $N(\text{CH}) = (0.35 \pm 0.015)N(\text{OH}) + 0.40 \pm 0.17$ (in 10^{13} cm^{-2}), in which the column density are calculated for the line-of-sight, not for different velocity components. The average abundance ratio of $N(\text{CH})/N(\text{OH})$ is 0.40 ± 0.06 .

Li et al. (2018a) presented OH column density $N(\text{OH})$ of decomposed velocity components toward the sightlines in this work. By comparing the same velocity components, we found that most CH components satisfy $N(\text{CH}) < N(\text{OH})$ except for two, T0526+24 centering at 7.2 km s^{-1} and T0629+10 centering at 4.7 km s^{-1} . The $N(\text{CH})/N(\text{OH})$ ratios of the two components are 6.4 ± 5.2 and 10.8 ± 6.5 , implying an overabundance of CH in these two clouds. This phenomenon of enhanced

CH abundance was also detected toward the source HD 34078 in Weselak et al. (2009) and will be discussed in the section 5.1. When these two velocity components are excluded, the $N(\text{CH})/N(\text{OH})$ ratio of the 9 clouds ranges from 0.06 to 0.83 with an average value of 0.44 ± 0.28 .

As shown in the Figure 7, the relationship between $N(\text{CH})$ and $N(\text{OH})$ shows a tight correlation for the 9 clouds. Due to the presence of uncertainties in both $N(\text{CH})$ and $N(\text{OH})$, we introduced the Orthogonal Distance Regression (ODR) method instead of Ordinary Least Square fitting to fit the relationship. The column density of CH and OH could be linearly fitted with the following formula, $\log N(\text{CH}) = (1.80 \pm 0.49) \log N(\text{OH}) - 11.59 \pm 6.87$. After excluding 3 data points whose uncertainty value is larger than their data value, the ODR fit for the rest 6 data points is $\log N(\text{CH}) = (1.76 \pm 0.64) \log N(\text{OH}) - 10.99 \pm 8.92$. This means that the 3 data points with large uncertainties contribute little to the trend of CH-OH relationship.

We combine the results with explicit measurement from Liszt & Lucas (2002), Weselak et al. (2009, 2010), and this work to construct a full sample of 32 points, in which the abnormal 3 points are excluded. The $N(\text{CH})/N(\text{OH})$ ratio of this sample is 0.43 ± 0.18 . After adopting ODR method, the relationship between CH and OH could be fitted with $\log N(\text{CH}) = (0.89 \pm 0.09) \log N(\text{OH}) + 1.06 \pm 1.21$. For comparison, the fit without uncertainty leads to $\log N(\text{CH}) = (1.08 \pm 0.17) \log N(\text{OH}) - 1.48 \pm 2.42$.

5.1. Overabundance of CH

As shown in section 5, the overabundance of CH exists. Due to the higher reaction rate of CH formation at higher temperature, increasing the kinematic temperature (e.g., $\sim 300 \text{ K}$) in PDR model with equilibrium chemistry could greatly increase $N(\text{CH})$. But this process would also accelerate the reaction rate of other species (e.g., OH, CO) (van Dishoeck & Black 1988).

Overabundant CH^+ has been observed by multiple observations (e.g., Sheffer et al. 2008). The overabundance of CH^+ is able to accelerate CH formation through the reaction $\text{CH}^+ + \text{e} \rightarrow \text{CH}$ or even faster reactions $\text{CH}^+ + \text{H}_2 \rightarrow \text{CH}_2^+ + \text{H}$ and $\text{CH}_2^+ + \text{e} \rightarrow \text{CH} + \text{H}$. However, the formation of CH^+ in the diffuse ISM is difficult since the reaction, $\text{C}^+ + \text{H}_2 \rightarrow \text{CH}^+ + \text{H}$, is endothermic with a rate of $1 \times 10^{-10} \exp(-4640/T_{\text{kin}}) \text{ cm}^{-3} \text{ s}^{-1}$ (Federman et al. 1996).

The nonequilibrium chemistry, single-fluid shock models (Elitzur & Watson 1978) is able to produce observed CH^+ abundance but results in overabundant OH. The two-fluid magnetohydrodynamic (MHD) shock (C-shock) model (Draine & Katz 1986a,b; Draine 1986)

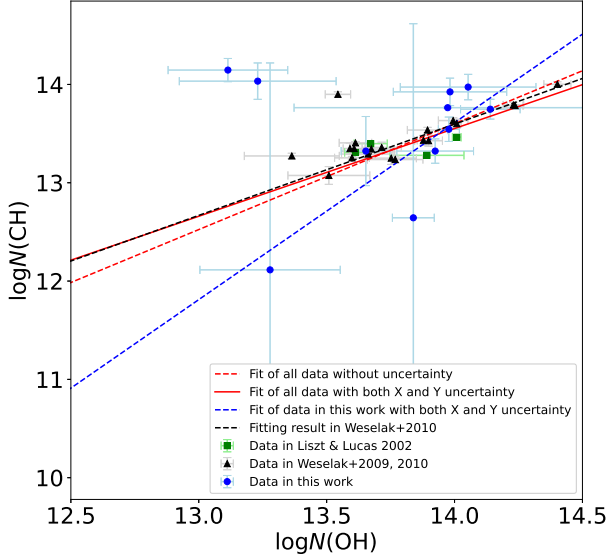


Figure 7. Relationship between $N(\text{CH})$ and $N(\text{OH})$. Compared to radio data in this paper, the data of Weselak et al. (2009, 2010) were obtained from visible spectra. The dashed black line represents the fitting result given in Weselak et al. (2010), in which the source HD 34078 (upper left in the figure) with enhanced CH abundance was not included. The blue dashed line represents fitting result of data in this work, in which the two clouds with overabundant CH (T0526+24 centering at 7.2 km s^{-1} and T0629+10 centering at 4.7 km s^{-1} , upper left in the figure) are excluded. The fitting result (red solid line) of all data does not include these 3 points.

was introduced to explain the CH^+ abundance problem. The main problem of this model is that the predicted velocity shift (5 km s^{-1} , Hawkins & Craig 1991) between CH^+ and CH absorption profile was not observed by high resolution observations (Gredel et al. 1993; Crane et al. 1995; Crawford 1995; Gredel 1997). Flower & Pineau des Forets (1998) claimed that the velocity shift could be less than 2 km s^{-1} from the C-shock model. With $n_{\text{H}} = 50 \text{ cm}^{-3}$, fractional ionization $n_{\text{e}}/n_{\text{H}} = 2.3 \times 10^{-4}$, magnetic field $B = 7.1 \mu\text{G}$ and UV intensity $\chi = 3$, the $N(\text{CH})/N(\text{OH})$ value reaches ~ 14 (Draine & Katz 1986b), which could explain the observed values in this work. Although no such shift was observed between the central velocities of OH and CH, one cannot rule out the shock origin of the CH and CH^+ over-abundance, considering the geometrical reliance of shock models. Xu & Li (2016) has found the C-shock model to be a probable explanation for over-abundant CH in the transition zone across the Taurus molecular cloud edge. Clearly, more systematic surveys and analyses are required to ascertain the role of shocks in CH excitation. The current and upcoming SKA precursors (ASKAP and MeerKAT in particular) and SKA-1

poise to fulfill such requirements. We particularly note the successor of Arecibo, the Five-hundred-meter Aperture Spherical radio Telescope (FAST: Li et al. 2018b, 2019). We are expanding the Millennium survey with FAST. The upper end of the FAST frequency coverage is currently at 1.5 GHz, but expected to be extended to 3.3 GHz in about a year. The improved sky-coverage and the sensitivity of FAST will facilitate substantial increase of HI, OH, and CH absorption measurements, over the Millennium survey.

6. CH VS. H_2

CO low- J rotational transitions fail to trace diffuse molecular gas and the so called “dark gas” (e.g. Grenier et al. 2005; Planck Collaboration et al. 2011) because of the low excitation and low abundance. Black & Dalgarno (1973) and Black et al. (1975) first investigated the chemical models leading to CH formation through reactions with H_2 . These models imply a close correlation between CH and H_2 , which was found to be consistent with observations (Federman 1982). Many efforts have been done to measure the relationship between column density of CH and H_2 in various environments. We summarized the results derived by a series of radio, visible, millimeter and sub-millimeter observations toward clouds with different environments:

1. By assuming $|T_{\text{ex}}| = -15 \text{ K}$, Sandell et al. (1981) found $N(\text{CH}) \approx 6 \times 10^{13} \text{ A}_{\text{B}}$ through 3335 MHz emission toward L1642.
2. With the assumption of $T_{\text{ex}} = -60 \text{ K}$, Mattila (1986) obtained the abundance $N(\text{CH})/N(\text{H}_2) = 4.0 \times 10^{-8}$ and correlation $\log N(\text{CH}) = (1.02 \pm 0.04) \log N(\text{H}_2) - 7.82$ based on 3335 MHz observations of low extinction clouds L134, L1780 and L1590. This relationship is valid for $10^{19.5} < N(\text{H}_2) < 10^{21.5} \text{ cm}^{-2}$ and breaks down for dense gas regions with $N(\text{H}_2) \gtrsim 3 \times 10^{22} \text{ cm}^{-2}$.
3. Based on 3264, 3335, and 3349 MHz emission data, Suutarinen et al. (2011) found that CH abundance in TMC1 ranges from 1.0×10^{-8} to $\sim 2.2 \times 10^{-8}$. The value $T_{\text{ex}}^{3335} = -10 \text{ K}$ was chosen to calculate $N(\text{CH})$.
4. Xu & Li (2016) investigated CH emission across the Taurus boundary and found $N(\text{CH})$ as a function of visual extinction A_{V} , $N(\text{CH}) = 2.6 \times 10^{13} \exp[-(\frac{A_{\text{V}} - 2.0}{1.0})^2] + 1.6 \times 10^{13} \text{ cm}^{-2}$. The assumption of $T_{\text{ex}}^{3335} = -60 \text{ K}$ was adopted when calculating $N(\text{CH})$.
5. Visible transitions of CH and Lyman $B - X$ transitions of H_2 provide direction measurement of

$N(\text{CH})$ and $N(\text{H}_2)$, respectively. Liszt & Lucas (2002) collected previous direct $N(\text{CH})$ and $N(\text{H}_2)$ measurements (Crane et al. 1995; Crawford 1995; Allen 1994; Gredel et al. 1993; Federman et al. 1994; Danks et al. 1984; van Dishoeck & Black 1989; Crutcher 1985; Jenniskens et al. 1992; Penprase 1993; Rachford et al. 2001; Savage et al. 1977) and found averaged CH abundance $X_{\text{CH}}=N(\text{CH})/N(\text{H}_2)=4.3 \pm 1.9 \times 10^{-8}$. In addition, the CH and H_2 relation follows $\log N(\text{CH}) = (1.00 \pm 0.06) \log N(\text{H}_2) - 7.35 \pm 1.31$.

With new visible and far-UV measurements, Sheffer et al. (2008) found $N(\text{CH})/N(\text{H}_2)=3.5_{-1.4}^{+2.1} \times 10^{-8}$. The average relationship between $N(\text{CH})$ and $N(\text{H}_2)$ for all data is $\log N(\text{CH}) = (0.97 \pm 0.07) \log N(\text{H}_2) - 6.80 \pm 1.50$. It is $\log N(\text{CH}) = (0.92 \pm 0.19) \log N(\text{H}_2) - 5.87 \pm 3.78$ when $\log N(\text{H}_2) < 20.4$ and $\log N(\text{CH}) = (1.09 \pm 0.19) \log N(\text{H}_2) - 9.34 \pm 3.90$ when $\log N(\text{H}_2) > 20.4$.

Traditionally, the proton column density was derived from $E(\text{B}-V)$ value through $N_{\text{H}} = 5.8 \times 10^{21} E(\text{B}-V)$ (Bohlin et al. 1978). More and more evidences present a higher conversion factor. By comparing precise $N(\text{H I})$ and $E(\text{B}-V)$ for pure atomic sightlines of Millennium survey, Nguyen et al. (2018) found the conversion, $N_{\text{H}} = (9.4 \pm 1.6) \times 10^{21} E(\text{B}-V)$, which is 62% higher compared to that in Bohlin et al. (1978). With adoption of this conversion value, it is able to derive total column density along sightline $N_{\text{H}}^{\text{LOS}}$ based on $E(\text{B}-V)$ measurement from Schlegel et al. (1998). The column density of all decomposed H I components are present in Heiles & Troland (2003b). In order to calculate total proton in the detected CH clouds, we subtracted $N(\text{H I})$ contribution of H I components that do not cover the velocity range of CH emission.

The column density of H_2 is calculated by $N(\text{H}_2) = (N_{\text{H}}^{\text{LOS}} - N^{\text{tot}}(\text{H I}))/2$, in which $N^{\text{tot}}(\text{H I})$ is total H I column density along sightline. As shown in the left panel of Figure 8, the relationship between $N(\text{CH})$ and $N(\text{H}_2)$ follows $\log N(\text{CH}) = (1.03 \pm 0.66) \log N(\text{H}_2) - 8.38 \pm 14.16$. Due to the limit of sample number, the slope of 1.03 ± 0.66 has a relative large uncertainty but is consistent with that derived from visible and far-UV absorptions (Liszt & Lucas 2002; Sheffer et al. 2008).

The right panel of Figure 8 shows the relationship between CH abundance $X(\text{CH})=N(\text{CH})/N(\text{H}_2)$ and $N(\text{H}_2)$. Only upper limit of $X(\text{CH})$ was derived toward the source 3C154. The mean value of $X(\text{CH})$ is $6.0 \pm 1.4 \times 10^{-8}$ toward other five sources (3C123, 3C131, 3C133, T0526+24, and T0629+10). It becomes

$3.5 \pm 0.4 \times 10^{-8}$ when the source T0526+24 ($X(\text{CH})=16.1 \pm 6.9 \times 10^{-8}$) is excluded. Though the mean $X(\text{CH})$ value of $3.5 \pm 0.4 \times 10^{-8}$ is highly consistent with $X(\text{CH})=3.5_{-1.4}^{+2.1} \times 10^{-8}$ in Sheffer et al. (2008), more statistical samples are necessary.

7. SUMMARY

We have performed high-sensitivity CH observations toward 18 extra-galactic continuum sources with the Arecibo telescope. The excitation temperature and optical depth of CH are obtained directly through ON/OFF observations. Combining with the existing OH, H I and extinction data, the main conclusions are as follows:

1. Although spreading in a wide range between -54.5 K to -0.5 K, 23% of the excitation temperatures of the CH 3335 MHz main line concentrate within $[-5, 0]$ K according to our Monte Carlo analysis (Figure 4 (a)). Compared to the adoption of $T_{\text{ex}} = -3$ K, $N(\text{CH})$ derived with $T_{\text{ex}} = -10$ K (Rydbeck et al. 1976) and $T_{\text{ex}} = -60 \pm 30$ K (Genzel et al. 1979) will be overestimated by a factor of 1.7 and 2.0, respectively.
2. The CH excitation temperatures can be described by a log-normal distribution,

$$f(x) = \frac{a}{(15 - T_{\text{ex}})\sigma} e^{-\frac{(\ln(15 - T_{\text{ex}}) - \mu)^2}{2\sigma^2}}. \quad (9)$$

The fitting values of a , μ and σ for 3335, 3264 and 3349 MHz lines are (1.7, 3.2, 0.4), (1.2, 3.0, 0.3) and (1.2, 3.1, 0.3) respectively.

3. The optical depth of 3335 MHz transition ranges from -33.5×10^{-3} to -2.9×10^{-3} (Figure 4 (b)), indicating that the CH emission is optically thin.
4. We derived accurate $N(\text{CH})$ value based on three transitions of CH. The value $N(\text{CH})$ will be underestimated by a factor of 1.32 ± 0.03 when only 3335 MHz data is adopted under the LTE condition (Figure 6).
5. In this study, $\log N(\text{CH})$ correlates linearly with $\log N(\text{OH})$ following $\log N(\text{CH}) = (1.80 \pm 0.49) \log N(\text{OH}) - 11.59 \pm 6.87$ for 9 data points. The relationship becomes $\log N(\text{CH}) = (0.89 \pm 0.09) \log N(\text{OH}) + 1.06 \pm 1.21$ for a full sample of 32 data points when previous results are included (Figure 7).
6. The average CH abundance relative to H_2 is $3.5 \pm 0.4 \times 10^{-8}$ when the source T0524+10 with large deviation is excluded. The relationship between

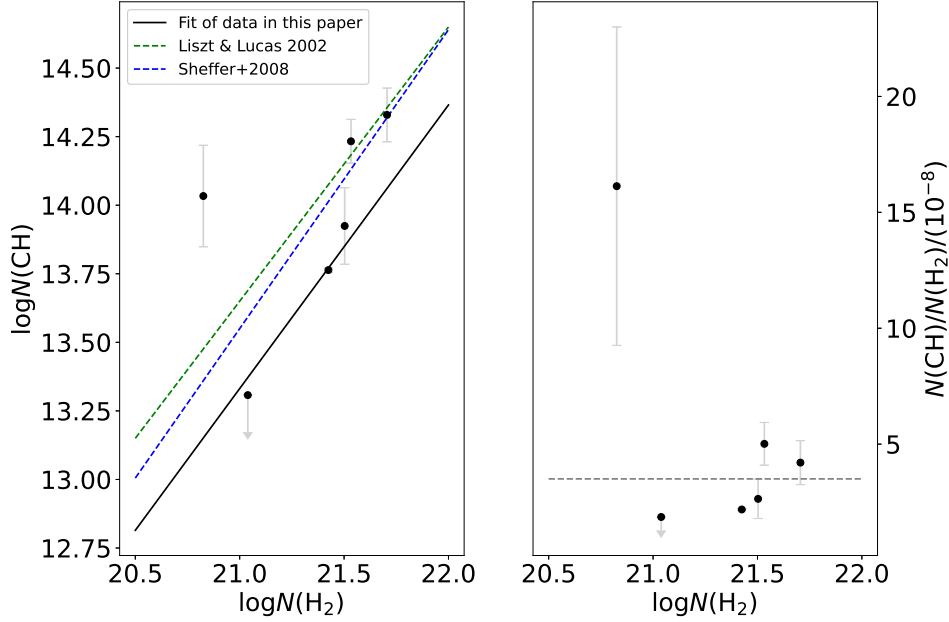


Figure 8. Relationship between $N(\text{CH})$ versus $N(\text{H}_2)$ (*Left panel*) and $N(\text{CH})/N(\text{H}_2)$ versus $N(\text{H}_2)$ (*Right panel*). The solid line in the left panel represents linear fitting result, $\log N(\text{CH}) = (1.03 \pm 0.66) \log N(\text{H}_2) - 8.38 \pm 14.16$. The source T0526+24 with significant deviation of $N(\text{CH})/N(\text{H}_2)$ was excluded during fitting. The green and blue dashed lines represent the fitted profile in Liszt & Lucas (2002) ($\log N(\text{CH}) = (1.00 \pm 0.06) \log N(\text{H}_2) - 7.35 \pm 1.31$) and Sheffer et al. (2008) ($\log N(\text{CH}) = (1.09 \pm 0.19) \log N(\text{H}_2) - 9.34 \pm 3.90$). The dashed line in the right panel represents the value of 3.5×10^{-8} . The point with upper limit is 3C154.

$N(\text{CH})$ and $N(\text{H}_2)$ is found to be $\log N(\text{CH}) = (1.03 \pm 0.66) \log N(\text{H}_2) - 8.38 \pm 14.16$, consistent with result from visible observations (Figure 8).

ACKNOWLEDGMENTS

We are grateful to the anonymous referee for the constructive suggestions, which have greatly improved this paper. We thank Chao-Wei Tsai for useful

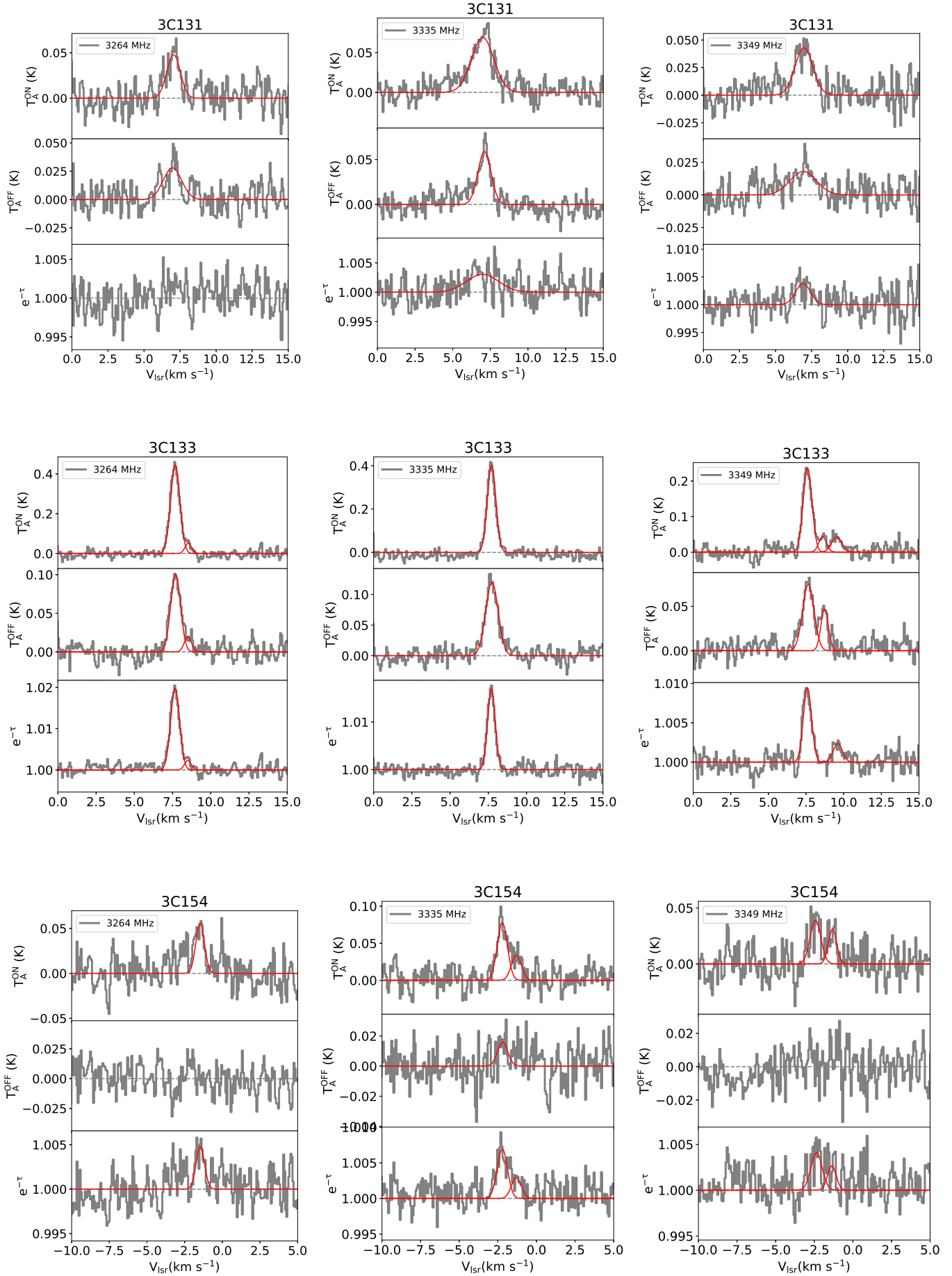
discussion. This work is supported by the National Natural Science Foundation of China (Grant No. 11988101, 11803051, 11725313, and 12033005), National Key R&D Program of China (2017YFA0402600 and 2018YFE0202900), CAS International Partnership Program (114A11KYSB20160008).

Finally, we would like to express our personal gratitude to the great Arecibo telescope, which bestowed upon us not only fantastic data, but also life-long inspiration.

REFERENCES

- Allen, M. M. 1994, *ApJ*, 424, 754. doi:10.1086/173928
- Black, J. H. & Dalgarno, A. 1973, *Astrophys. Lett.*, 15, 79
- Black, J. H., Dalgarno, A., & Oppenheimer, M. 1975, *ApJ*, 199, 633. doi:10.1086/153730
- Bohlin, R. C., Savage, B. D., & Drake, J. F. 1978, *ApJ*, 224, 132. doi:10.1086/156357
- Boissé, P., Le Petit, F., Rollinde, E., et al. 2005, *A&A*, 429, 509. doi:10.1051/0004-6361:20047135
- Crane, P., Lambert, D. L., & Sheffer, Y. 1995, *ApJS*, 99, 107. doi:10.1086/192180
- Crawford, I. A. 1995, *MNRAS*, 277, 458. doi:10.1093/mnras/277.2.458
- Crutcher, R. M. 1985, *ApJ*, 288, 604. doi:10.1086/162826
- Dailey, E. M., Smith, A. J., Magnani, L., et al. 2020, *MNRAS*, 495, 510. doi:10.1093/mnras/staa1188
- Danks, A. C., Federman, S. R., & Lambert, D. L. 1984, *A&A*, 130, 62
- Dickey, J. M., Kulkarni, S. R., van Gorkom, J. H., et al. 1983, *ApJS*, 53, 591. doi:10.1086/190903
- Dickey, J. M., Crovisier, J., & Kazes, I. 1981, *A&A*, 98, 271
- Draine, B. T. 1986, *ApJ*, 310, 408. doi:10.1086/164694
- Draine, B. T. & Katz, N. 1986, *ApJ*, 306, 655. doi:10.1086/164375
- Draine, B. T. & Katz, N. 1986, *ApJ*, 310, 392. doi:10.1086/164693

- Dunham, T. 1937, *PASP*, 49, 26. doi:10.1086/124759
- Elitzur, M. & Watson, W. D. 1978, *ApJL*, 222, L141.
doi:10.1086/182711
- Federman, S. R. 1982, *ApJ*, 257, 125. doi:10.1086/159970
- Federman, S. R., Strom, C. J., Lambert, D. L., et al. 1994, *ApJ*, 424, 772. doi:10.1086/173930
- Federman, S. R., Rawlings, J. M. C., Taylor, S. D., et al. 1996, *MNRAS*, 279, L41. doi:10.1093/mnras/279.3.L41
- Felenbok, P. & Roueff, E. 1996, *ApJL*, 465, L57.
doi:10.1086/310129
- Flower, D. R. & Pineau des Forets, G. 1998, *MNRAS*, 297, 1182. doi:10.1046/j.1365-8711.1998.01574.x
- Genzel, R., Downes, D., Pauls, T., et al. 1979, *A&A*, 73, 253
- Gredel, R. 1997, *A&A*, 320, 929
- Gredel, R., van Dishoeck, E. F., & Black, J. H. 1993, *A&A*, 269, 477
- Grenier, I. A., Casandjian, J.-M., & Terrier, R. 2005, *Science*, 307, 1292. doi:10.1126/science.1106924
- Hawkins, I. & Craig, N. 1991, *ApJ*, 375, 642.
doi:10.1086/170227
- Heiles, C. & Troland, T. H. 2003, *ApJS*, 145, 329.
doi:10.1086/367785
- Heiles, C. & Troland, T. H. 2003, *ApJ*, 586, 1067.
doi:10.1086/367828
- Hjalmarson, A., Sume, A., Elider, J., et al. 1977, *ApJS*, 35, 263. doi:10.1086/190480
- Jacq, T., Baudry, A., Despois, D., et al. 1987, *A&A*, 173, 347
- Jacob, A. M., Menten, K. M., Wiesemeyer, H., et al. 2021, *A&A*, 650, A133. doi:10.1051/0004-6361/202140419
- Jenniskens, P., Ehrenfreund, P., & Desert, F.-X. 1992, *A&A*, 265, L1
- Lang, K. R. & Wilson, R. F. 1978, *ApJ*, 224, 125.
doi:10.1086/156356
- Li, D., Xu, D., Heiles, C., et al. 2015, *Publication of Korean Astronomical Society*, 30, 75.
doi:10.5303/PKAS.2015.30.2.075
- Li, D., Tang, N., Nguyen, H., et al. 2018a, *ApJS*, 235, 1.
doi:10.3847/1538-4365/aaa762
- Li, D., Wang, P., Qian, L., et al. 2018b, *IEEE Microwave Magazine*, 19, 112. doi:10.1109/MMM.2018.2802178
- Li, D., Dickey, J. M., & Liu, S. 2019, *Research in Astronomy and Astrophysics*, 19, 016.
doi:10.1088/1674-4527/19/2/16
- Liszt, H. & Lucas, R. 2002, *A&A*, 391, 693.
doi:10.1051/0004-6361:20020849
- Litvak, M. M. 1969, *ApJ*, 156, 471. doi:10.1086/149982
- Lucas, R. & Liszt, H. 1996, *A&A*, 307, 237
- Luo, G., Li, D., Tang, N., et al. 2020, *ApJL*, 889, L4.
doi:10.3847/2041-8213/ab6337
- Magnani, L., Sandell, G., & Lada, E. A. 1992, *A&AS*, 93, 509
- Magnani, L. & Onello, J. S. 1993, *ApJ*, 408, 559.
doi:10.1086/172613
- Magnani, L., Onello, J. S., Adams, N. G., et al. 1998, *ApJ*, 504, 290. doi:10.1086/306062
- Mattila, K. 1986, *A&A*, 160, 157
- McKellar, A. 1940, *PASP*, 52, 187. doi:10.1086/125159
- Nguyen, H., Dawson, J. R., Miville-Deschênes, M.-A., et al. 2018, *ApJ*, 862, 49. doi:10.3847/1538-4357/aac82b
- Penprase, B. E. 1993, *ApJS*, 88, 433. doi:10.1086/191829
- Rachford, B. L., Snow, T. P., Tumlinson, J., et al. 2001, *ApJ*, 555, 839. doi:10.1086/321489
- Roueff, E. 1996, *MNRAS*, 279, L37.
doi:10.1093/mnras/279.3.L37
- Rydbeck, O. E. H., Kollberg, E., Hjalmarson, A., et al. 1976, *ApJS*, 31, 333. doi:10.1086/190385
- Sakai, N., Maezawa, H., Sakai, T., et al. 2012, *A&A*, 546, A103. doi:10.1051/0004-6361/201219106
- Sandell, G., Johansson, L. E. B., Rieu, N. Q., et al. 1981, *A&A*, 97, 317
- Sandell, G., Hoglund, B., & Friberg, P. 1980, *A&A*, 83, 226
- Sandell, G., Magnani, L., & Lada, E. A. 1988, *ApJ*, 329, 920. doi:10.1086/166436
- Savage, B. D., Bohlin, R. C., Drake, J. F., et al. 1977, *ApJ*, 216, 291. doi:10.1086/155471
- Schlegel, D. J., Finkbeiner, D. P., & Davis, M. 1998, *ApJ*, 500, 525. doi:10.1086/305772
- Sheffer, Y., Rogers, M., Federman, S. R., et al. 2008, *ApJ*, 687, 1075. doi:10.1086/591484
- Suutarinen, A., Geppert, W. D., Harju, J., et al. 2011, *A&A*, 531, A121. doi:10.1051/0004-6361/201016079
- Swings, P. & Rosenfeld, L. 1937, *ApJ*, 86, 483.
doi:10.1086/143880
- Planck Collaboration, Ade, P. A. R., Aghanim, N., et al. 2011, *A&A*, 536, A19. doi:10.1051/0004-6361/201116479
- van Dishoeck, E. F. & Black, J. H. 1988, *ApJ*, 334, 771.
doi:10.1086/166877
- van Dishoeck, E. F. & Black, J. H. 1989, *ApJ*, 340, 273.
doi:10.1086/167391
- Weselak, T., Galazutdinov, G. A., Beletsky, Y., et al. 2010, *MNRAS*, 402, 1991. doi:10.1111/j.1365-2966.2009.16028.x
- Weselak, T., Galazutdinov, G., Beletsky, Y., et al. 2009, *A&A*, 499, 783. doi:10.1051/0004-6361/200911616
- Xu, D. & Li, D. 2016, *ApJ*, 833, 90.
doi:10.3847/1538-4357/833/1/90
- Zuckerman, B. & Turner, B. E. 1975, *ApJ*, 197, 123.
doi:10.1086/153492



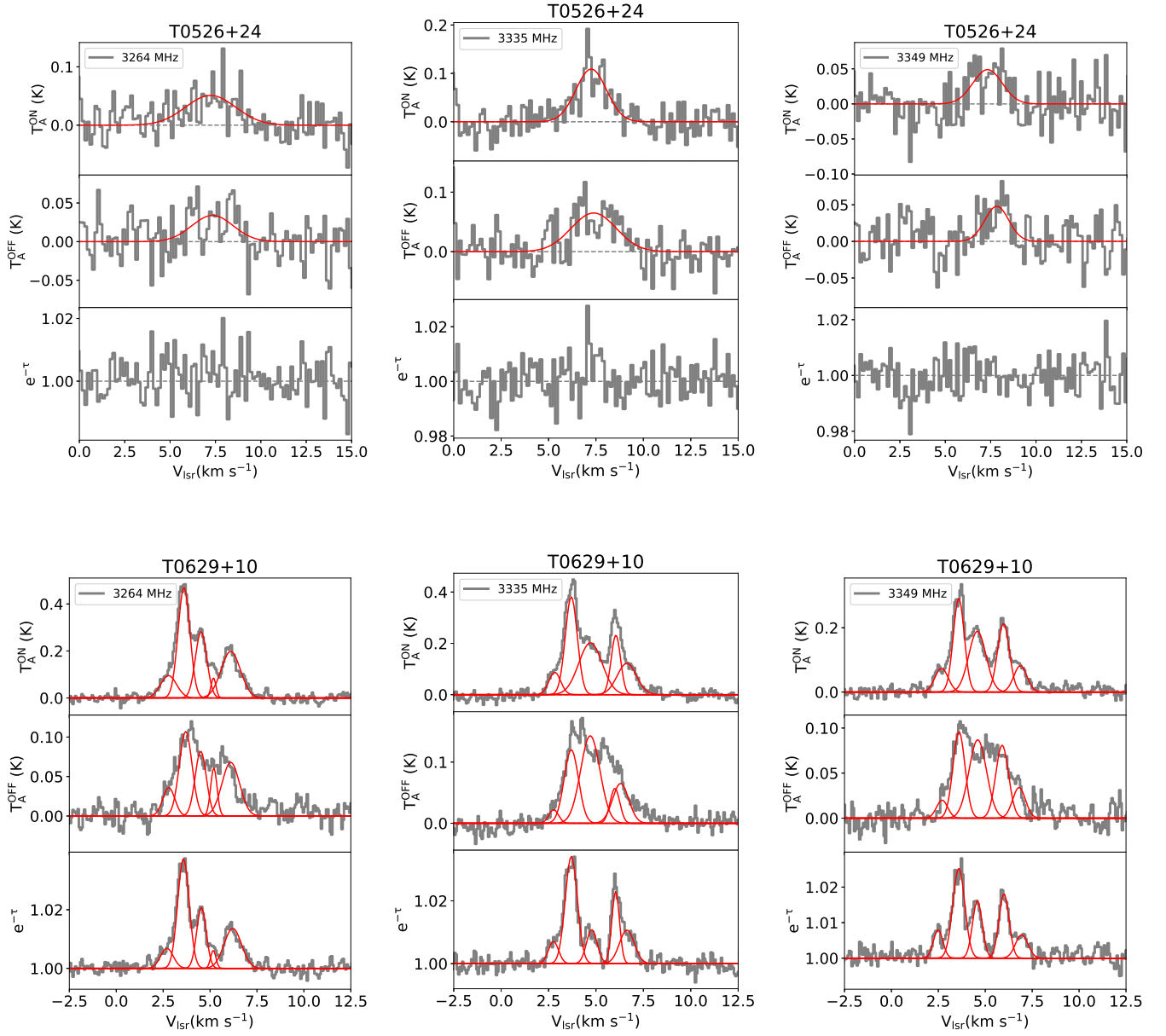


Figure 9. Spectra and Gaussian decomposition components of 3C131, 3C133, 3C154, T0526+24 and T0629+10. The description of each panel is same with that in the Figure 3.

Table 1. Gaussian fitting parameters of CH 3335 MHz data.

Source	l/b	CH 3335 MHz							
		V_{cen}	ΔV	T_{C}	τ	T_{ex}	$N(\text{CH})_{3335}^{\text{LTE}}$	$N(\text{CH})$	$N(\text{OH})$
		($^{\circ}$)	(km s^{-1})	(km s^{-1})	(K)	(10^{-3})	(K)	(10^{13}cm^{-2})	(10^{13}cm^{-2})
3C123	170.6/−11.7	4.0 (0.2)	1.47 (0.27)	9.23e2	−2.9 (0.1)	−54.5 (12.1)	7.1(2.1)	...	1.13(0.69)
3C123	170.6/−11.7	4.5 (0.0)	0.46 (0.03)	9.23e2	−11.0 (0.1)	−10.5 (2.9)	1.6 (0.5)	2.1 (0.6)	0.84(0.29)
3C123	170.6/−11.7	5.5 (0.1)	0.94 (0.08)	9.23e2	−4.5 (0.1)	−33.2 (6.8)	4.2(0.9)	5.6 (1.3)	1.38(0.37)
3C131	171.4/−7.8	7.0 (0.0)	1.76 (0.10)	5.88	−3.1 (0.5)	−38.9 (10.3)	6.3(2.0)	8.4(2.7)	0.96(0.49)
3C133	177.7/−9.9	7.7 (0.0)	0.65 (0.02)	1.72e1	−16.9 (0.5)	−13.3 (2.4)	4.4(0.8)	5.8(1.1)	0.94(1.30)
3C154	185.6/4.0	−2.2 (0.1)	0.77 (0.12)	9.89	−7.0 (0.8)	−0.4 (3.3)	0.1(0.5)	...	0.19(0.12)
3C154	185.6/4.0	−1.3 (0.1)	0.76 (0.27)	9.89	−0.7 < τ < 0	−92.6 < T_{ex} < 0	< 1.5	...	0.18(0.21)
T0526+24	181.4/−5.2	7.2 (0.1)	1.90 (0.23)	5.89	−7.5 (1.4)	−18.9 (7.0)	8.1(3.5)	10.8 (4.6)	0.17(0.12)
T0629+10	201.5/0.5	2.8 (0.1)	0.73 (0.12)	8.62	−7.1 (0.9)	−6.4 (4.1)	1.0 (0.7)	1.3 (0.9)	...
T0629+10	201.5/0.5	3.7 (0.0)	0.74 (0.05)	8.62	−33.5 (0.9)	−3.6 (1.0)	2.7 (0.8)	3.5 (1.0)	0.95(0.09)
T0629+10	201.5/0.5	4.7 (0.1)	1.45 (0.22)	8.62	−10.7 (0.9)	−22.5 (4.8)	10.5 (2.9)	14.0 (3.8)	0.13(0.07)
T0629+10	201.5/0.5	6.0 (0.0)	0.58 (0.06)	8.62	−22.7 (3.6)	−0.9 (4.1)	0.36 (1.63)	0.44 (2.00)	0.69(0.13)
T0629+10	201.5/0.5	6.6 (0.2)	1.20 (0.26)	8.62	−10.6 (1.1)	−4.2 (3.2)	1.6 (1.3)	2.1(1.7)	0.45(0.10)

Table 2. Gaussian fitting parameters of CH 3264 and 3349 MHz data.

Source	l/b	CH 3264 MHz					CH 3349 MHz				
		V_{cen}	ΔV	T_{C}	τ	T_{ex}	V_{cen}	ΔV	T_{C}	τ	T_{ex}
	($^{\circ}$)	(km s^{-1})	(km s^{-1})	(K)	(10^{-3})	(K)	(km s^{-1})	(km s^{-1})	(K)	(10^{-3})	(K)
3C123	170.6/−11.7	1.05e2	3.4 (0.1)	0.65 (0.15)	9.13e1	−1.2 (0.2)	−43.7 (36.8)
3C123	170.6/−11.7	4.4 (0.0)	0.68 (0.03)	1.05e2	−7.2 (0.0)	−17.3 (2.7)	4.3 (0.0)	0.67 (0.04)	9.13e1	−6.3 (0.2)	−22.0 (9.5)
3C123	170.6/−11.7	5.5 (0.0)	0.90 (0.07)	1.05e2	−3.9 (0.1)	−10.0 (5.5)	5.4 (0.0)	0.97 (0.07)	9.13e1	−3.4 (0.1)	−32.4 (11.6)
3C131	171.4/−7.8	7.0 (0.1)	1.10 (0.13)	8.24	−2.4 (0.4)	−26.0 (8.0)	7.0 (0.1)	1.46 (0.14)	5.77	−3.8 (0.9)	−11.0 (6.6)
3C133	177.7/−9.9	7.7 (0.0)	0.71 (0.02)	1.79e1	−19.6 (0.5)	−8.5 (1.8)	7.6 (0.0)	0.69 (0.03)	1.69e1	−9.5 (0.5)	−17.1 (3.7)
3C133	177.7/−9.9	8.5 (0.1)	0.50 (0.12)	1.79e1	−2.3 (0.6)	−7.9 (13.2)	8.6 (0.1)	0.60 (0.18)	1.69e1	0.2 (0.3)	664.7 (1034.9)
3C133	177.7/−9.9	1.79e1	9.5 (0.1)	0.80 (0.19)	1.69e1	−0.9 < τ < 0	−68.5 < T_{ex} < 0
3C154	185.6/4.0	−1.5 (0.0)	0.67 (0.10)	1.10e1	−2.6 < τ < 0	−22.8 < T_{ex} < 0	−1.3 (0.1)	0.63 (0.17)	9.73	−0.4 < τ < 0	−161.4 < T_{ex} < 0
3C154	185.6/4.0	1.10e1	−2.4 (0.1)	0.82 (0.16)	9.73	−1.2 < τ < 0	−51.9 < T_{ex} < 0
T0526+24	181.4/−5.2	7.2 (0.3)	3.24 (0.22)	6.03	−2.8 (1.3)	−27.3 (21.5)	7.3 (0.2)	1.90 (0.14)	5.87	−0.2 (1.9)	−701.6 (7910.1)
T0629+10	201.5/0.5	2.8 (0.1)	1.00 (0.22)	1.07e1	−6.8 (0.8)	−5.3 (4.4)	2.7 (0.1)	0.83 (0.13)	8.51	−8.0 (0.9)	0.9 (2.7)
T0629+10	201.5/0.5	3.6 (0.0)	0.74 (0.05)	1.07e1	−36.7 (0.8)	−1.9 (0.8)	3.6 (0.0)	0.69 (0.04)	8.51	−25.0 (0.8)	−4.7 (1.2)
T0629+10	201.5/0.5	4.5 (0.0)	0.71 (0.06)	1.07e1	−20.5 (0.8)	−4.4 (1.6)	4.6 (0.0)	1.08 (0.10)	8.51	−16.0 (0.9)	−5.3 (1.9)
T0629+10	201.5/0.5	5.2 (0.0)	0.31 (0.06)	1.07e1	−6.1 (1.2)	−5.3 (6.9)	6.0 (0.0)	0.74 (0.05)	8.51	−17.9 (0.8)	−5.4 (1.6)
T0629+10	201.5/0.5	6.1 (0.0)	1.21 (0.05)	1.07e1	−13.6 (0.6)	−6.7 (2.0)	6.9 (0.1)	0.82 (0.12)	8.51	−6.6 (0.8)	−7.1 (4.0)